The Astrophysical Journal, 994:243 (11pp), 2025 December 1 https://doi.org/10.3847/1538-4357/ae11a0

On the Distance to the Black Hole X-Ray Binary Swift J1727.8–1613

Benjamin J. Burridge[1], James C. A. Miller-Jones[1], Arash Bahramian[1], Steve R. Prabu[1,2], Reagan Streeter[1], Noel Castro Segura[3], Jesús M. Corral-Santana[4], Christian Knigge[5], Andrzej Zdziarski[6], Daniel Mata Sánchez[7,8], Evangelia Tremou[9], Francesco Carotenuto[10], Rob Fender[2], and Payaswini Saikia[11]

[1] International Centre for Radio Astronomy Research, Curtin University, GPO Box U1987, Perth WA 6845, Australia; benjamin.burridge@icrar.org
[2] Astrophysics, Department of Physics, University of Oxford, Keble Road, Oxford, OX1 3RH, UK
[3] Department of Physics, University of Warwick, Gibbet Hill Road, Coventry CV4 7AL, UK
[4] European Southern Observatory, Alonso de Córdova 3107, Casilla 19001 Vitacura, Santiago, Chile
[5] School of Physics & Astronomy, University of Southampton, Southampton SO17 1BJ, UK
[6] Nicolaus Copernicus Astronomical Center, Polish Academy of Sciences, Bartycka 18, PL-00-716 Warszawa, Poland
[7] Instituto de Astrofísica de Canarias, E-38206 La Laguna, Tenerife, Spain
[8] Departamento de Astrofísica, Univ. de La Laguna, E-38206 La Laguna, Tenerife, Spain
[9] National Radio Astronomy Observatory, Socorro, NM 87801, USA
[10] INAF-Osservatorio Astronomico di Roma, Via Frascati 33, I-00076, Monte Porzio Catone (RM), Italy
[11] Center for Astrophysics and Space Science, New York University Abu Dhabi, P.O. Box 129188, Abu Dhabi, UAE

Received 2025 February 9; revised 2025 September 3; accepted 2025 September 28; published 2025 November 28

Abstract

We review the existing distance estimates to the black hole X-ray binary Swift J1727.8–1613, present new radio and near-UV spectra to update the distance constraints, and discuss the accuracies and caveats of the associated methodologies. We use line-of-sight H I absorption spectra captured using the MeerKAT radio telescope to estimate a maximum radial velocity with respect to the local standard of rest of $24.8 \pm 2.8\ \mathrm{km\,s^{-1}}$ for Swift J1727.8−1613, which is significantly lower than that of a nearby extragalactic reference source. From this, we derive a near-kinematic distance of $d_{\rm near} = 3.6 \pm 0.3$ (stat) $\pm\, 2.3$ (sys) kpc as a lower bound after accounting for additional uncertainties given its Galactic longitude and latitude, $(l, b) \approx (8.6^\circ, 10.3^\circ)$. Near-UV spectra from the Hubble Space Telescope's Space Telescope Imaging Spectrograph allows us to constrain the line-of-sight color excess to $E(B - V) = 0.37 \pm 0.01$ (stat) $\pm\, 0.025$ (sys). We then implement this in Monte Carlo simulations and present a distance to Swift J1727.8−1613 of $5.5^{+1.4}_{-1.1}$ kpc, under the assumption that the donor star is an unevolved, main-sequence K4(±1) V star. This distance implies a natal kick velocity of $190 \pm 30\ \mathrm{km\,s^{-1}}$ and therefore an asymmetrical supernova explosion within the Galactic disk as the expected birth mechanism. A lower distance is implied if the donor star has instead lost significant mass during the binary evolution. Hence, more accurate measurements of the binary inclination angle or donor star rotational broadening from future observations would help to better constrain the distance.

Unified Astronomy Thesaurus concepts: Black hole physics (159); Distance measure (395); X-ray binary stars (1811); Radio transient sources (2008); Neutral hydrogen clouds (1099); Interstellar reddening (853)

Materials only available in the online version of record: data behind figure

1. Introduction

Distance is an important parameter in the study of all astrophysical objects. For Galactic low-mass X-ray binaries (XRBs), accurate distances allow for better estimation of other parameters, such as the peak Eddington luminosity ($L_{\rm Edd}$) fraction (ELF) and jet parameters including physical size scales, inclination angles, and speeds.

Reliably measuring the distance to newly discovered XRBs can be challenging. For instance, across the different phases of an outburst, the system's luminosity can fluctuate, often in and out of detectable levels. This inconsistent detectability can preclude the measurements required for accurate distance determination.

1.1. Distance Methods

Distance determination techniques applicable to XRBs can be broadly categorized into three groups: (1) astrometric or kinematic methods; (2) approaches that use observations of the donor star, X-ray source, or jets; or (3) techniques based on propagation effects. We summarize these in Sections 1.1.1–1.1.3. We then discuss in more detail the two techniques that we employ that exploit the relationships between the distance and H I absorption in radio observations (Section 1.1.4) and the color excess or reddening, $E(B - V)$, as measured using near-UV observations (Section 1.1.5).

1.1.1. Astrometry and Kinematics

High-significance XRB parallax measurements with Gaia (Gaia Collaboration et al. 2016; P. Atri et al. 2019; P. Gandhi et al. 2019; R. M. Arnason et al. 2021) or very long baseline interferometry (VLBI) at radio wavelengths (e.g., J. C. A. Miller-Jones et al. 2009, 2021; M. J. Reid et al. 2011, 2014a; P. Atri et al. 2020; M. J. Reid & J. C. A. Miller-Jones 2023) are the gold standard for measuring distances to Galactic XRBs. However, radio parallaxes can be impeded by line-of-sight scatter broadening for XRBs located in the Galactic plane (GP). In fact, extinction in the GP and the faintness of quiescent XRBs precludes Gaia distances in many cases. Given the typical kiloparsec distances of XRBs, sub-milliarcsecond precision is required (B. E. Tetarenko et al. 2016).

These methods also require observations that span an extended timeframe, which is not always possible for XRB outbursts.

Alternatively, kinematic distance methodologies use measured proper motions and velocities predicted using the Galactic rotation model to infer the most likely distance. Despite relying on the assumption of low peculiar velocities relative to the local standard of rest (LSR), these can provide reliable distances in some circumstances (M. J. Reid 2022) and can be useful for XRBs (e.g., V. Dhawan et al. 2007; M. J. Reid & J. C. A. Miller-Jones 2023).

1.1.2. Stellar, X-Ray, and Jet Observations

One can use optical spectroscopy of the XRB donor star to estimate the distance (e.g., G. Dubus et al. 2001; P. G. Jonker & G. Nelemans 2004; P. Charles et al. 2019). With measured values for the donor star's absolute and apparent magnitudes and the extinction along the line of sight, one can use the distance modulus (e.g., D. Mata Sánchez et al. 2024, 2025) to infer the distance via

$$d = 10^{(m-M-A+5)/5}, \tag{1}$$

where d is the distance, m is the apparent magnitude, M is the absolute magnitude, and A is the extinction.

Obscuration of optical light is pronounced for targets residing in the GP due to increased interstellar dust, making donor stars difficult to identify, and introducing additional uncertainty to the distance modulus equation. However, for targets outside the GP, extinction can be harder to estimate accurately.

X-ray luminosities of XRB outbursts during soft-to-hard and hard-to-intermediate state transitions have been observed to occur at somewhat consistent ELFs, albeit with factor of $\sim$3 scatter in these measurements (E. Kalemci et al. 2013; B. E. Tetarenko et al. 2016; A. Vahdat Motlagh et al. 2019). X-ray studies during these transitions allow one to compare the measured and expected intrinsic luminosities and thereby estimate the distance (e.g., Y. Abdulghani et al. 2024).

Further X-ray methods exist, including the combination of X-ray spectroscopy and the distance dependency of accretion disk spectral fits, which R. I. Hynes et al. (2002) applied to constrain the distance to XTE J1859+226. Additionally, C. R. Powell et al. (2007) used the timescale of outburst decay X-ray light curves to estimate the absolute luminosity at a characteristic time and therefore provide a measure of the distance.

In the radio band, the proper motions of two-sided jets can be combined to place an upper limit on the source distance (e.g., I. F. Mirabel & L. F. Rodríguez 1994).

1.1.3. Propagation and the Interstellar Medium

X-rays produced by XRB flares will propagate outwards and may subsequently scatter off intervening interstellar dust clouds. Provided the distances to these dust clouds can be determined, one can combine this information with analysis of the time delays and intensities of these expanding X-ray dust scattering rings to measure the distance to the source (e.g., S. Heinz et al. 2015; A. P. Beardmore et al. 2016; G. Lamer et al. 2021).

X-ray absorption features in observed spectra can be used to measure the hydrogen column density, $N_{\rm H}$. When coupled with hydrogen distribution models, one can infer the distance to the source.

The relation between $E(B-V)$ and the aforementioned extinction along the line of sight can be used to inform distance modulus calculations (e.g., E. F. Schlafly & D. P. Finkbeiner 2011). The inverse relation between $E(B-V)$ and the distance therefore allows constraints on one to constrain the other. We examine and implement this method in Sections 1.1.5 and 4.2, respectively.

Lastly, line-of-sight H I absorption has long been used as an XRB distance estimator (e.g., J. M. Dickey 1983; F. J. Lockman et al. 2007; J. Chauhan et al. 2019, 2021). We explore this method further in Section 1.1.4 below and apply it in Sections 2.1, 3.1, and 4.1.

1.1.4. H I Absorption

Our first distance method uses H I absorption, which can be observed when clouds of neutral hydrogen along the line of sight absorb the broadband continuum emission produced by the target at the H I frequency in their rest frame. These clouds move with different velocities relative to us along the line of sight, due to the rotation of the Milky Way, as well as other effects such as noncircular streaming motions that we assume to be minimal. The more clouds that are intersected by the line of sight, the more H I absorption features that are imprinted at different frequencies on the observed radio spectrum. One benefit of H I absorption over parallax is that the required data can be gathered within a much shorter timeframe; a single observation can suffice should the observed source be particularly bright.

The Doppler-shifted frequencies can be converted into LSR velocities and compared to the Milky Way rotation curve. The maximum velocity occurs at the tangent point, where the rotational velocity is entirely along the line of sight. Identical velocities are seen on either side of this maximum, giving rise to an ambiguity in mapping observed absorption velocities to distances within the solar circle. A maximum observed velocity that is less than the tangent point velocity could correspond to a near-kinematic distance before the tangent point or a far kinematic distance beyond the tangent point (e.g., T. V. Wenger et al. 2018, Figure 4).

To resolve this kinematic distance ambiguity, one must observe the target but also at least one extragalactic reference source close enough to the target in the sky such that any differences in the anticipated H I distributions along the lines of sight are minimized. The emission from the reference source will have passed through all Galactic H I clouds along the line of sight, with clouds outside the solar circle imprinting absorption velocities of the opposite sign. Any absorption present in the reference spectrum but absent in the target spectrum then allows us to place an upper limit on the distance.

1.1.5. $E(B-V)$

Our second distance method relies on the reddening caused by interstellar dust preferentially scattering shorter wavelengths. This can be determined by subtracting the observed difference between blue and visible magnitudes, B and V, to quantify the reddening along the line of sight.

$E(B-V)$ can be calculated using various relations between it and interstellar absorption lines (e.g., U. Munari &

T. Zwitter 1997; G. Wallerstein et al. 2007), or $N_{\rm H}$ (e.g., D. Mata Sánchez et al. 2025). It can be estimated from Galactic dust maps, both two-dimensional (2D; e.g., D. J. Schlegel et al. 1998; Y.-K. Chiang 2023) and three-dimensional (3D; e.g., G. M. Green et al. 2019; G. Edenhofer et al. 2024). Near-UV spectra can also be used as implemented in Sections 2.2 and 3.2.

With a value for $E(B-V)$, one can derive the extinction. For example, it is common to use $R_V = 3.1$ as a Galactic average with

$$A_V = R_V\, E(B-V) \tag{2}$$

to convert reddening to the total extinction along the line of sight or vice versa (B. D. Savage & J. S. Mathis 1979; E. L. Fitzpatrick 2004). When combined with measurements of absolute and apparent magnitudes in Equation (1), the distance can then be calculated.

1.2. Swift J1727.8−1613

Swift J1727.8−1613 (J1727), located at $(l, b) = (8.641502°, 10.254899°)$, was first detected as an X-ray transient on 2023 August 4 (H. Negoro et al. 2023). Bright radio emission was observed within a couple of days (J. C. A. Miller-Jones et al. 2023b), which continued to brighten through early September (J. Bright et al. 2023). Analysis of observations in late August and early September revealed a bright core and a large two-sided, asymmetrical jet (C. M. Wood et al. 2024). Radio monitoring in early October suggested radio quenching and subsequent flaring (J. C. A. Miller-Jones et al. 2023a).

This event was deemed a low-mass XRB outburst (A. J. Castro-Tirado et al. 2023), and its high radio brightness made J1727 a suitable target for H I absorption measurements. Since then, the compact object has been dynamically confirmed to be a black hole (BH; D. Mata Sánchez et al. 2025, hereafter MS25).

Further studies of the outburst revealed that it produced relativistic jets that are the largest resolved jets in an XRB to date (C. M. Wood et al. 2024). The ejection of transient jets in J1727 has also been shown to have occurred simultaneously with a bright X-ray flare and a sudden change in the X-ray properties of the accretion inflow (C. M. Wood et al. 2025).

The Gaia optical counterpart for Swift J1727.8−1613 currently has proper motion but no parallax. A VLBI radio parallax will not be possible with the observations taken to date, as the XRB has already returned to the quiescent state.

1.2.1. Current Distance Estimates

Y. Abdulghani et al. (2024) estimated a distance of $1.52^{+0.85}_{-0.61}$ kpc from a Bayesian approach of soft-state X-ray modeling. This appeared to align with A. Veledina et al. (2023), who used X-ray flux scaling arguments to provide an early estimate of approximately 1.5 kpc. However, Y. Abdulghani et al. (2024) concede that their distance estimate may be underestimated by up to ∼70%, given that only soft-state data and no state-transition information was used.

D. Mata Sánchez et al. (2024, hereafter MS24) used donor star magnitudes in conjunction with various relations in the literature to derive values for the parameters in Equation (1). These included the relation between the interstellar Ca II doublet (H and K) and the distance to early-type stars per A. Megier et al. (2009). This was calibrated using objects within a few hundred parsecs from the GP (up to 450 pc), slightly below but still consistent with their final inferred height for J1727. The authors also used the relations between the equivalent widths of the interstellar line K I 7699 Å and diffuse interstellar band at 8621 Å and $E(B-V)$ per U. Munari & T. Zwitter (1997) and G. Wallerstein et al. (2007), respectively. However, these relations resulted in particularly large values for $E(B-V)$ at 0.8 ± 0.3 and 0.9 ± 0.3, respectively. Lastly, the relation between hydrogen column density $N_{\rm H}$ and V-band extinction A_V per T. Güver & F. Özel (2009) was combined with Equation (2) to infer $E(B-V) = 0.47 \pm 0.13$. These values of $E(B-V)$ cover a wide range, and some have large associated uncertainties, which propagate to the distance constraints. We discuss this further in Section 4.2.1 using our near-UV results and Galactic dust maps.

Following the above, MS24 calculated the weighted mean of the resulting distances to be $d = 2.7 \pm 0.3$ kpc. MS25 then directly measured the orbital period, $P_{\rm orb}$, and reported the best-fitting spectral type template of K4(±1)V for a donor star that is partially veiled by the accretion disk. Using this, they revised the absolute r-band magnitude to $M_r = 6.6 \pm 0.5$ mag. They also measured an apparent r-band magnitude of $m_r = 21.13 \pm 0.05$ mag and presented an updated consolidated weighted mean distance of $d = 3.4 \pm 0.3$ kpc.

1.2.2. Contents

In Section 2, we detail the methods used and data obtained. In Section 3, we present our H I absorption and near-UV spectra. In Section 4, we discuss the interpretation of our results in constraining the distance to J1727, along with various caveats and implications for natal kick velocities and ELFs. In Section 5, we present our suggested distance to J1727.

2. Observations and Data Reduction

2.1. MeerKAT Radio Data

We observed J1727 as part of the The Hunt for Dynamic and Explosive Radio Transients with MeerKAT[12] (ThunderKAT; R. Fender et al. 2016) large survey project and its successor, X-KAT (PI: Fender).

We conducted 1–2 GHz (L-band) radio observations of the J1727 field using the South African Square Kilometre Array precursor radio telescope, MeerKAT (F. Camilo 2018), between 2023 August 27 and October 16. Our measured flux densities for J1727 were in the range 50–837 mJy due to radio flaring of the source. Further details of these observations are provided in Table 1.

All observations were performed with the L-band receiver—two using MeerKAT's standard "32k" mode and two using the "32k zoom" mode, hereafter referred to as "32k-S" and "32k-Z," respectively. While each mode contains 32,768 channels, the 32k-Z mode has channel bandwidths that are 8 times smaller and thus provides an eightfold increase in frequency resolution. We alternated our observation scans between J1727 and the phase calibrator, PKS J1733−1304

---

[12] http://science.uct.ac.za/thunderkat

Table 1
A Summary of MeerKAT Observation Parameters

MJD	Observation Start Date (dd-mm-yyyy)	Observation Start Time (hh:mm:ss)	Exposure Time (mm:ss)	*L*-band Mode	Centre Frequency (MHz)	Total Bandwidth (MHz)	Channel Width (kHz)	J1727 Peak Flux Density (mJy)
60183	27-08-2023	15:27:59.6	14:55.6	Standard	1283.9869	856	26.123	49.7 ± 0.2
60193	06-09-2023	15:06:32.1	14:56.9	Zoom	1419.9984	107	3.265	97.5 ± 0.4
60231	14-10-2023	12:40:20.2	14:55.6	Standard	1283.9869	856	26.123	836.6 ± 2.3
60233	16-10-2023	15:50:13.8	14:56.9	Zoom	1419.9984	107	3.265	104.3 ± 0.4

Note. All times are in Coordinated Universal Time. The uncertainties on the peak flux densities are the rms noise in the continuum image of the J1727 field.

(J1733 hereafter), with a single scan of the bandpass and flux calibrator J1939−6342 in each observation.

Having obtained MeerKAT observations of J1727 during which it was sufficiently bright (i.e., $\gtrsim$50 mJy) at 1.4 GHz, we compute H I absorption spectra by processing the radio data to create a radio spectrum that includes the frequency of the H I spectral line, $f_{\rm HI} = 1420.30575177$ MHz. We convert Doppler shifts in frequency to line-of-sight LSR velocities. We then compare the maximum positive or negative velocity observed in the resulting spectra with the Milky Way rotation curve to generate estimates of the kinematic distance via the source code for the Kinematic Distance Calculation Tool[13,14] (KDCT; T. V. Wenger 2018).

2.1.1. Reference Source Selection

Due to the lack of bright ($\gtrsim$50 mJy) extragalactic background sources in the field, i.e., within 1° of J1727, we used the bright ($S_0 \approx 6$ Jy) phase calibrator J1733 to derive our reference H I absorption spectra. With J1733 located at $(l, b) \approx (12.03°, 10.81°)$, the two fields are only 3.4° apart, primarily in Galactic longitude. As J1733 is extragalactic, observations allow us to probe the full set of H I clouds along a nearby line of sight (see also Section 4.1.2 regarding H I scale height).

2.1.2. Data Reduction

We undertook all data reduction on the Ilifu research cloud infrastructure managed by the Inter-university Institute for Data Intensive Astronomy.[15] To streamline the processing of our H I data, we used the ThunderKAT H I Pipeline.[16] Simultaneously, we used Cube Analysis and Rendering Tool for Astronomy (A. Comrie et al. 2024) to interrogate the data.

The ThunderKAT H I Pipeline has three stages, each with its own bash script that employs several PYTHON scripts.

At a high level, the first stage of the pipeline uses Common Astronomy Software Applications (CASA Team et al. 2022) to retrieve the data for specified fields from the full observation measurement set and create separate files for each source. The pipeline then undoes previously applied flags to ensure H I spectral lines are not erroneously flagged as radio-frequency interference. The measurement set for each field is then converted into the `fits` format required for the MIRIAD software (R. J. Sault et al. 1995) used in the next stage.

The second and most computationally intensive stage begins with data preprocessing, and a region is defined to search for the position of the peak continuum emission. The target and calibrators' fields are defined, the reference antenna is set, and basic flagging is done. The H I spectral line frequency is added to the header information to convert frequency to velocity. Bandpass and gain calibrations are applied to the target field, and spectral cubes are made and cleaned for the target and defined reference source(s). A second-order polynomial is then fitted to the broadband radio continuum emission of each source and subtracted in frequency space to remove the continuum emission. The resulting residuals are used to create image cubes for each source, from which the spectra are extracted and written to ASCII files, ready for the final stage.

The third stage plots the target and reference spectra. The noise in each channel is used to give an estimation of absorption uncertainties in the velocity bins. In the event that there are multiple target or reference spectra to be combined, these are "stacked" to create weighted mean spectra and increase the signal-to-noise ratio (SNR). The absorption in each velocity bin is calculated from each spectrum weighted according to the inverse square of the noise.

2.2. Hubble Space Telescope Near-UV Spectroscopy

We obtained high-resolution near-UV spectroscopy with the Space Telescope Imaging Spectrograph (STIS; B. E. Woodgate et al. 1998) on board the Hubble Space Telescope (HST) in early 2023 October (MJD ~ 60219) during the outburst (program ID 16489; N. Castro Segura et al. 2020). We used E230M gratings with 200 s followed by 220 s exposures at the central wavelengths 1978 and 2707 Å, respectively, to cover the region $\lambda\lambda \simeq 1800$–3200 Å with a resolving power of $R = 30{,}000$. The data were reduced using the HST pipeline CALSTIS.[17]

3. Results

3.1. Radio

3.1.1. High-resolution 32k Zoom Mode

Both H I spectra from our two 32k-Z observations are displayed in the bottom two plots of Figure 1. Significant ($>3\sigma$) H I absorption toward J1727 is observed out to an estimated maximum LSR velocity $v_{\rm LSR} = 18.7 \pm 0.4$ km s^{-1} as shown in the inset for the mean weighted 32k-Z spectrum at the bottom left of Figure 2, using half the bin width as the

---

[13] http://www.treywenger.com/kd/

[14] http://github.com/tvwenger/kd

[15] http://idia.ac.za/ilifu-research-cloud-infrastructure/

[16] http://github.com/tremou/thunderkat_hi_pipeline.git

[17] Provided by the Space Telescope Science Institute: https://github.com/spacetelescope.

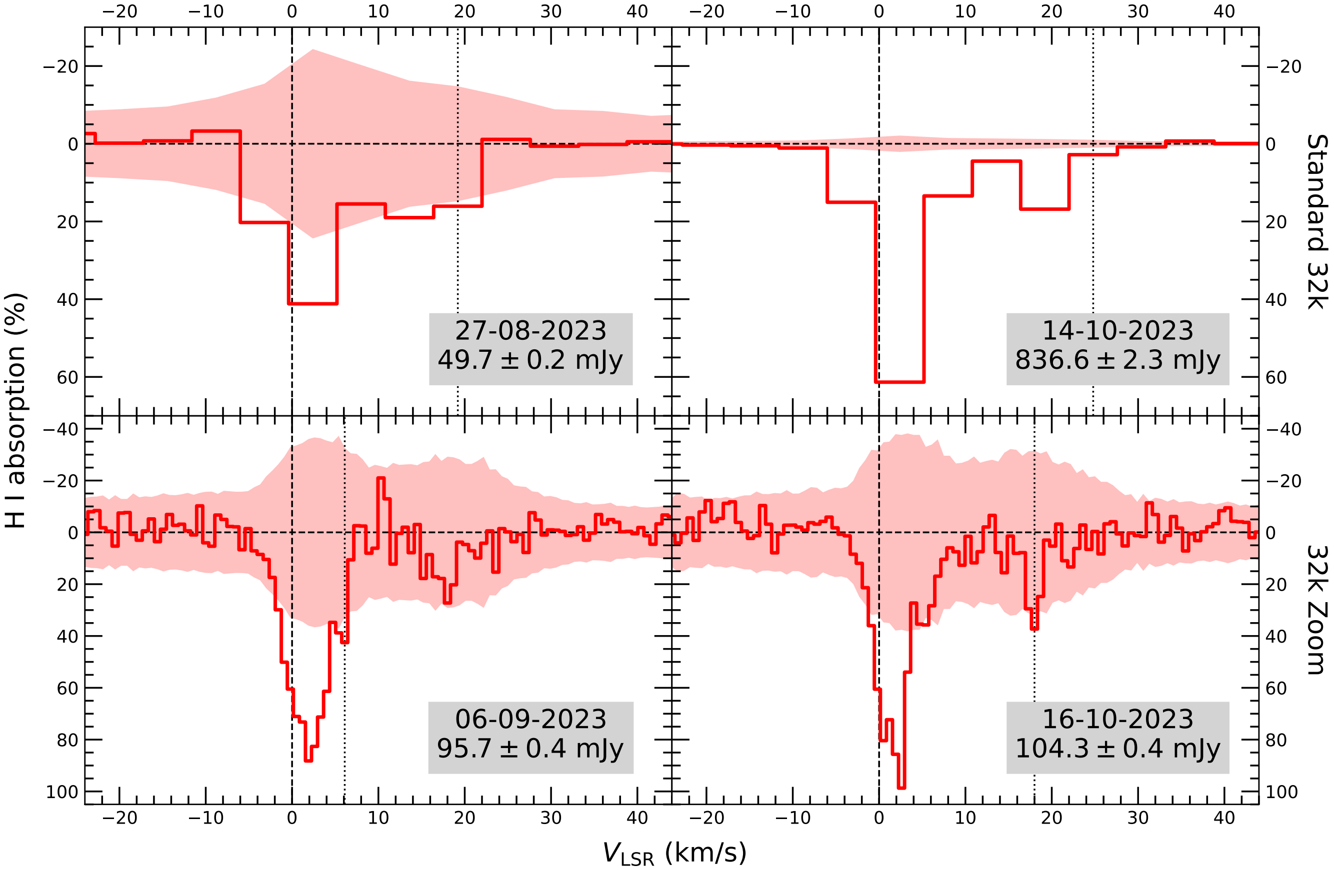

Figure 1. Our H I absorption spectra along of the line of sight toward J1727. The top two plots are the 32k-S spectra, and the bottom two plots are the 32k-Z spectra, with LSR velocity bin widths that are 5.6 and 0.7 km s^{-1} wide, respectively. The dashed lines indicate the origins of the *x*- and *y*-axes. The *y*-axis represents the residuals after subtracting the continuum emission from the data, with 3σ uncertainties indicated by the shaded areas, both of which are presented as a percentage of the continuum flux density of the source. The vertical dotted lines indicate the maximum velocity taken as the midpoint of the bin at which significant ($>3\sigma$) absorption is observed. In chronological order, these maximum velocities are 19.2 ± 2.8, 6.1 ± 0.4, 24.8 ± 2.8, and 18.0 ± 0.4 km s^{-1}. The significantly greater SNR of the 14 October 2023 spectrum meant we were able to observe significant ($>3\sigma$) H I absorption to greater velocities than observed in the 32k-Z spectra.

velocity uncertainty. The maximum absorption is observed to be ≈90%.

3.1.2. Standard 32k Mode

The effect of J1727's variable luminosities over the period of observations is seen in the differing SNR between our H I spectra from 27 August 2023 and 14 October 2023 shown in Figure 1. For 14 October 2023, we measured a J1727 peak flux density that was more than 8 times greater than either of our 32k-Z observations due to radio flaring, as observed by J. C. A. Miller-Jones et al. (2023a). The 14 October 2023 spectrum shows H I absorption at greater velocities than the 32k-Z spectra, albeit with greater bin widths. We therefore update our estimate of the maximum velocity of significant H I absorption toward J1727 to $v_{\rm LSR} = 24.8 \pm 2.8$ km s^{-1} as seen in the top-left inset in Figure 2. The maximum absorption is observed to be ≈61% for the 32k-S spectra, which is smaller than that of the 32k-Z spectra as the absorption is averaged over the wider velocity bin width.

3.1.3. Reference Source

Figure 2 compares H I absorption spectra toward J1727 and J1733. The latter is consistently much brighter, with flux densities exceeding 6 Jy. It also exhibits H I absorption to greater velocities (i.e., 32.7 ± 0.4 km s^{-1} in the 32k-Z spectrum), which is in line with J1733 being extragalactic. With an extragalactic point of comparison that is nearby in terms of sky location and with H I absorption to greater velocities, we infer that J1727 is closer than the tangent point and use the near-kinematic distance as a lower limit.

3.2. Near-UV

We determined the line-of-sight extinction to J1727 using the J. A. Cardelli et al. (1989) reddening law to fit a reddened power law representing the outer accretion disk to the near-UV spectrum as displayed in Figure 3. To estimate the errors, we performed a Monte Carlo simulation yielding $E(B-V) = 0.37 \pm 0.01$ (stat) ± 0.025 (sys), corresponding to $A_V \simeq 1.15$ per Equation (2) with $R_V = 3.1$. Given we use *r*-band magnitudes when calculating Equation (1), we derive the *r*-band extinction using $A_r = 2.271\, E(B\text{–}V) = 0.84 \pm 0.06$ (for Pan-STARRS1; E. F. Schlafly & D. P. Finkbeiner 2011).

4. Discussion

4.1. Kinematic Distance Constraint

Absorption features in the final H I spectra informed our use of the KDCT to generate kinematic distance estimates. We clearly observe greater velocities toward J1733 than J1727, as shown in Figure 2.

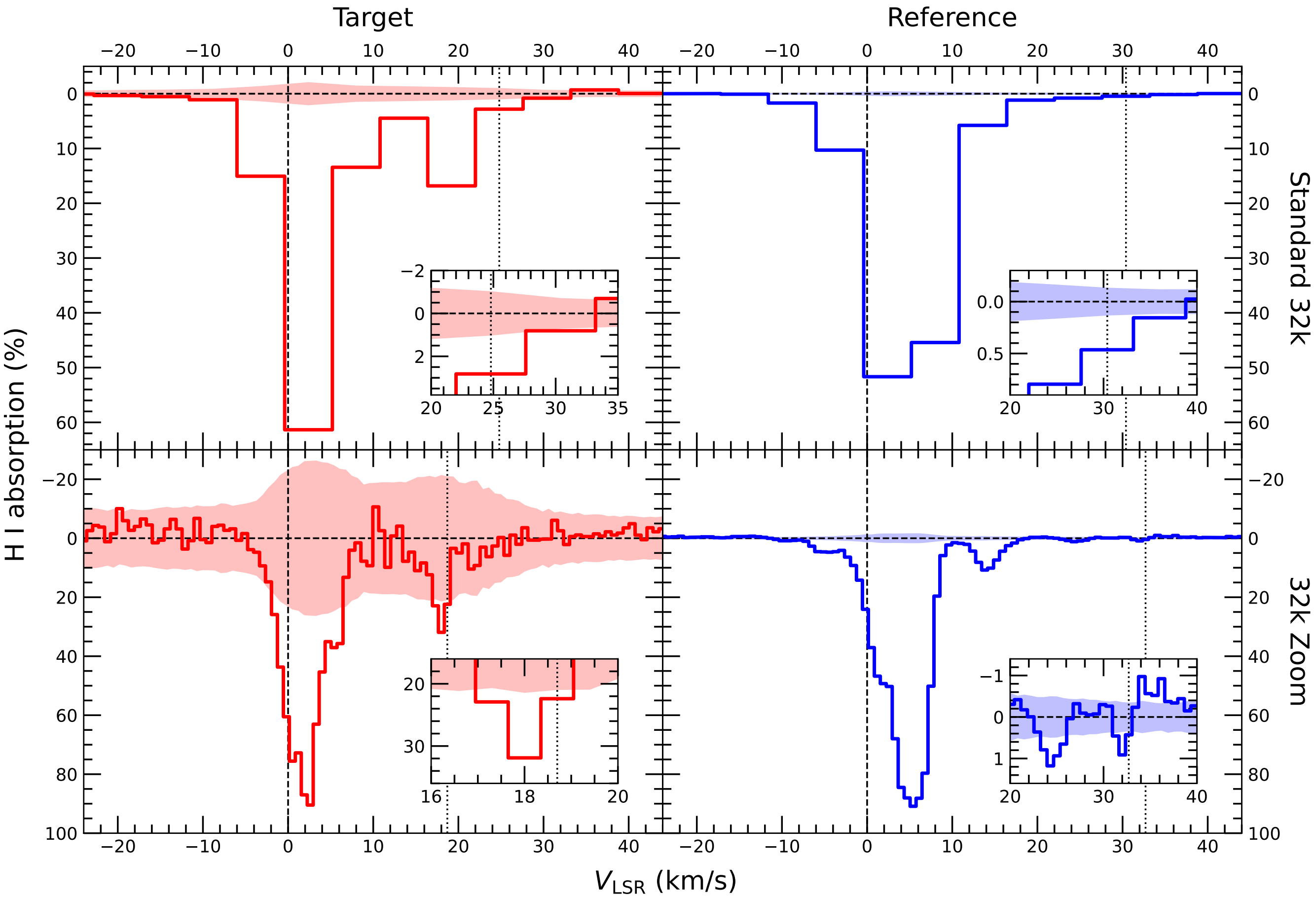

Figure 2. A consolidated view of the H I spectra for both the target, J1727 (red, left), and our reference source, J1733 (blue, right). We observed no significant ($>3\sigma$) absorption outside the velocities chosen as the x-axis range. The y-axis represents the H I absorption percentage. The dashed lines indicate the x- and y-axes' origins. The vertical dotted lines indicate the maximum velocity at which significant absorption is observed. For J1727, these are 24.8 ± 2.8 and 18.7 ± 0.4 km $\mathrm{s^{-1}}$. For J1733, these are 30.4 ± 2.8 and 32.7 ± 0.4 km $\mathrm{s^{-1}}$. The top-left plot is the 32k-S spectrum for J1727 from 14 October 2023, while the bottom-left plot is the mean weighted J1727 spectrum achieved by combining both 32k-Z spectra from Figure 1. We generated the 32k-Z (32k-S) spectra for J1733 from observations on 6 September 2023 (14 October 2023) with the peak J1733 flux density measured to be 6.1 ± 0.1 Jy (6.0 ± 0.1 Jy), providing the significantly greater SNR compared to that of the J1727 observations.

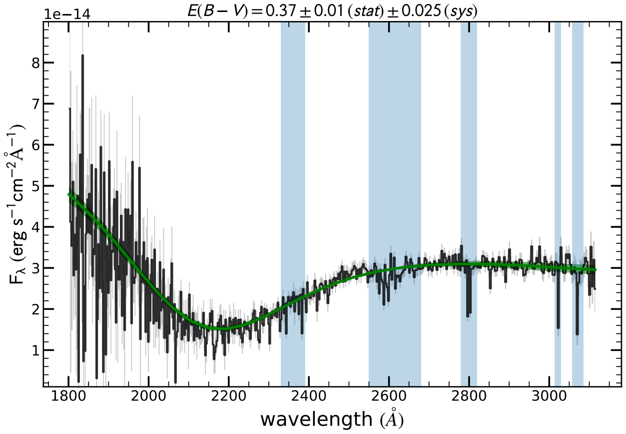

Figure 3. The near-UV spectrum of J1727 as seen by HST/STIS (black), with a reddened power-law fit (green) to the data (Castro Segura et al. 2025, in preparation) The uncertainty around the fit is indicated as a shaded region. The vertical shaded regions were masked during the fit to avoid Fe and Mg lines that may influence the fit.

We used our maximum H I absorption velocity and its uncertainty as inputs to the KDCT (T. V. Wenger et al. 2018), using their Method C and applying the revised solar motion parameters from M. J. Reid et al. (2014b) and the rotation curve from M. J. Reid et al. (2019). The total revised LSR velocity uncertainty includes measurement and systematic uncertainties such as noncircular streaming motions.

We amended the KDCT source code to resample the input and Galactic rotation curve parameters 10^7 times to minimize the Monte Carlo error. Results include Monte Carlo samples of d_{near}, d_{tan} (tangent point kinematic distance), and $v_{\mathrm{LSR,tan}}$ (tangent point LSR velocity). We estimate and report the median values as best estimates and the boundaries of the highest-density 68% interval as the uncertainties on these quantities. We repeated this process using inputs from 32k-Z and 32k-S H I absorption spectra.

The quantities d_{tan} and $v_{\mathrm{LSR,tan}}$ depend only on the source location. For J1727, we therefore estimate $d_{\mathrm{tan}} = 8.20 \pm 0.03$ kpc and $v_{\mathrm{LSR,tan}} = 93.9 \pm 3.3\ \mathrm{km\,s^{-1}}$. As d_{near} depends on the input velocity, we use our higher-SNR result of $24.8 \pm 2.8\ \mathrm{km\,s^{-1}}$ from our 32k-S spectra to estimate $d_{\mathrm{near}} = 3.6 \pm 0.3$ kpc.

4.1.1. Caveats

J1727 has a longitude close to the Galactic center (GC) and a relatively high Galactic latitude, leading to larger systematic uncertainties on the kinematic distance.

Regions within 15° in Galactic longitude from the GC feature increased H I emission from the GC (P. M. W. Kalberla & J. Kerp 2009), which leads to higher sky temperatures around the H I line and hence increased uncertainty in each spectral channel. At these longitudes, the motion of objects intersected by the line of sight is mostly perpendicular to the line of sight. Distances are thus inferred from a smaller spread in circular rotation velocities and subject to larger uncertainties, and so this region was excised from the study of T. V. Wenger et al. (2018).

More recently, G. H. Hunter et al. (2024) conducted numerical 2D hydrodynamical simulations to account for potential causes of Milky Way deviations from axisymmetry and gas cloud deviations from the circular rotation curve. The authors categorize these deviations into (i) random fluctuations around the average streaming motions that do not change the average velocity; and (ii) systematic changes in streaming velocity due to nonaxisymmetry, such as spiral arms and the Galactic bar. The authors then define regions of their simulated the Milky Way where the discrepancy between the kinematic and true distance is significant (>27%). Within $2 < d < 5$ kpc, the longitude for J1727 appears to correspond to a median absolute relative kinematic distance error of $|d_\mathrm{k} - d_\mathrm{true}|/d_\mathrm{true} \approx 63\%$. For $5 < d < 10$ kpc, this error reduces to approximately $12 \pm 8\%$. We use the greater 63% error above to expand the 1σ uncertainty on our measured kinematic distance, which becomes 3.6 ± 0.3 (stat) $\pm$ 2.3 (sys) kpc.

We observe that minor changes in Galactic longitudes close to the GC have major impacts on the values of d_near calculated using the KDCT. Specifically, J1733 has a maximum H I absorption velocity that is more than 30% greater than that of J1727; however, its larger Galactic longitude of $l \approx 12°$ results in a similar predicted value of d_near.

Our conservative lower limit of 3.6 ± 0.3 (stat) $\pm$ 2.3 (sys) kpc by accounting for longitudinal effects may therefore be reasonable, given the high Galactic latitude of J1727 and thus diminishing H I density along the lines of sight toward J1727 and J1733.

4.1.2. Scale Height of Galactic H I

The kinematic distance method works best for sources located in the GP where $b \approx 0$. T. V. Wenger et al. (2018) assumed a latitude of $b = 0$ and only use latitude to correct the LSR velocity with updated solar motion parameters. Having used 2D simulations, G. H. Hunter et al. (2024) assumed that the gas is integrated along the z-axis (vertically) and that the acceleration of the gas due to the Galactic potential is computed as if the gas lies in the GP with Galactic elevation, z, equal to zero. High Galactic latitudes correspond to greater Galactic elevations where less gas and other matter reside. Observed absorption features are primarily due to the gas clouds that are closer to us, as evidenced by the absence of detectable H I absorption out to the tangent point toward J1733. The impact of the Galactic latitude for J1727 will therefore lead to, if anything, an underestimation of the distance.

We do not observe H I absorption to the tangent point velocity of 93.9 ± 3.3 km s^{-1} in any of our spectra, only up to a maximum velocity 32.7 ± 0.4 km s^{-1} in the direction of J1733. This suggests that the line of sight has not intersected H I clouds at greater distances due to z increasing and H I density decreasing with distance. The distance lower bound of $d_\mathrm{near} = 3.6 \pm 0.3$ (stat) $\pm$ 2.3 (sys) kpc corresponds to a GP elevation of $z \approx 650 \pm 410$ pc.

P. M. W. Kalberla & J. Kerp (2009) suggest that the scale height of Milky Way's H I disk is approximately 150 pc at $R = 0$. The flaring and warping of the H I disk discussed by the authors would not be significant at the location of J1727 given it resides within the solar circle. More recently, D. R. Rybarczyk et al. (2024) showed the Gaussian-distributed thickness of the cold neutral medium in the solar neighborhood, σ_z, to be no more than ∼150 pc. It can therefore be expected that the majority of H I clouds along the lines of sight toward our sources will be contained within a few multiples of this σ_z. D. R. Rybarczyk et al. (2024) also found that H I features at $|b| > 5°$ trace primarily local structures, within 2 kpc. From their Figure 7, we see that the maximum H I absorption that we observed toward J1727 and J1733 falls into a region of outliers in Galactic position–velocity space, lending credence to our decision to impose additional uncertainty on our kinematic distance lower limit.

4.1.3. Feasibility of H I Absorption XRB Distances

Given the constraints made possible from a small number of XRB observations with MeerKAT, kinematic distances via H I absorption studies have the potential to form the basis of a rapid, routine, and reasonably accurate method for placing informative limits on the distances to Galactic transients, especially those situated within the GP and/or farther from the GC than J1727. This method will become increasingly powerful when used in conjunction with Square Kilometre Array observations of sufficiently bright XRBs in outburst, albeit with the caveats discussed above.

4.2. E(B − V) Distance Constraint

4.2.1. E(B − V) Validation

To first validate our result of $E(B–V) = 0.37 \pm 0.01$ (stat) $\pm$ 0.025 (sys) as derived from near-UV observations in Section 3.2, we compute the change in $E(B - V)$ along the line of sight to J1727 using Galactic dust maps. We present these results in Figure 4. Our results imply that $E(B - V)$ cannot be much greater than 0.4, as we run out of dust along the line of sight (but note the spatial resolution of dust maps could be a limiting factor). In fact, our best value for $E(B–V)$ is lower than all those estimated by MS24.

We note that while there is no evidence for intrinsic variability in N_H, the values used in studies of J1727 have varied from as low as $1.2 \pm 0.2 \times 10^{21}$ cm^{-2} (K. Chatterjee et al. 2024) to as high as $(4.1 \pm 0.1) \times 10^{21}$ cm^{-2} (P. A. Draghis et al. 2023), with other values in between (B. O'Connor et al. 2023; J.-Q. Peng et al. 2024; J. Svoboda et al. 2024). These discrepancies are likely due to the instrumental systematics and/or modeling choices differing from study to study.

MS24 used $(3.2 \pm 0.9) \times 10^{21}$ cm^{-2}, derived as the mean N_H value from B. O'Connor et al. (2023) and P. A. Draghis et al. (2023). The latter was estimated using the TBABS X-ray absorption model and the J. Wilms et al. (2000) abundances of elements. Both were derived by fitting observations made in late 2023 August, when the source was in the rising hard/hard-intermediate state.

We instead use $(2.4 \pm 0.1) \times 10^{21}$ cm^{-2} per J. Svoboda et al. (2024), which was derived using NICER, NuSTAR, and IXPE observations made during the soft state. The broad spectral coverage of this data set and the well-characterized disk blackbody spectrum during the soft state allows for a more

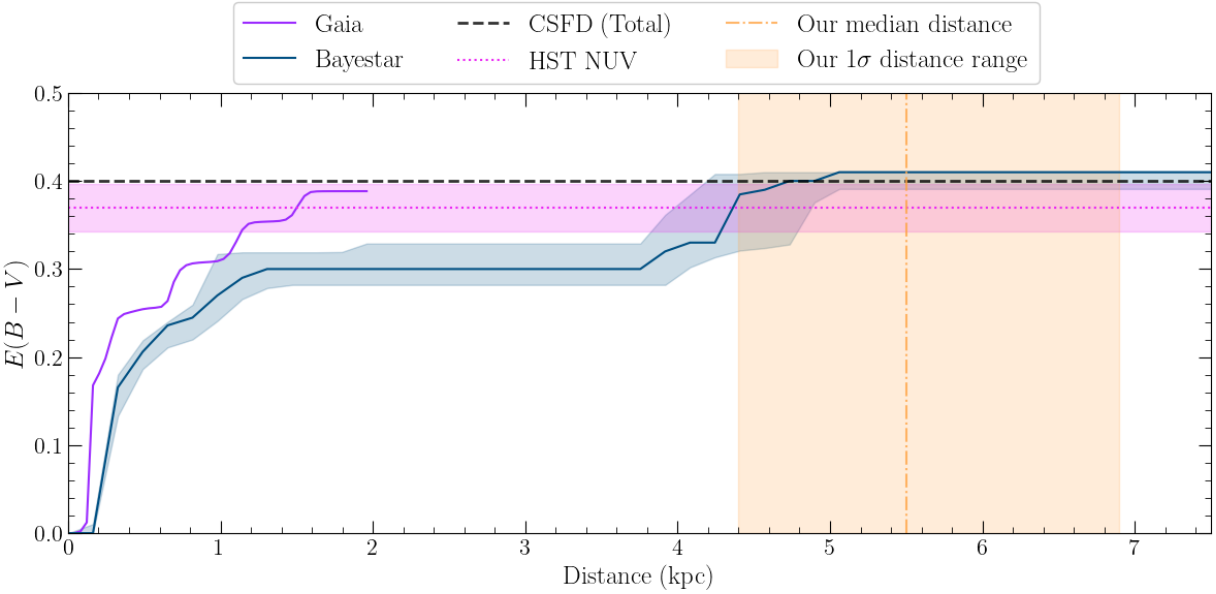

Figure 4. Estimates of $E(B-V)$ for distances between 0 and 7.5 kpc along the line of sight to J1727. The 3D Galactic dust maps include Bayestar (blue line; G. M. Green et al. 2019) and Gaia (purple line; G. Edenhofer et al. 2024). We also use an update of the 2D "SFD" dust map (D. J. Schlegel et al. 1998) to remove extragalactic contamination that is referred to as the "corrected SFD" (CSFD; gray dashed line; Y.-K. Chiang 2023). To investigate the likely maximum $E(B-V)$ values within this distance range, we use CSFD; as this only reports the total value for $E(B-V)$ along the line of sight, it serves as a good estimate of the maximum $E(B-V)$ in the direction of J1727 at high distances. From this, we derive a maximum $E(B-V) \approx 0.4$. Despite each having significant caveats and the disagreement between Bayestar and Gaia in how gas is distributed along the line of sight, both appear to accumulate to roughly this maximum value. Lastly, our estimate of $E(B-V)$ (pink dotted line) is derived from our near-UV observations. We use this estimate to conclude that values of $E(B-V) \gg 0.4$ may not be reliable and suggest a distance to J1727 of $5.5^{+1.4}_{-1.1}$ kpc with 1σ uncertainties, which are included for reference (orange dotted–dashed line and shaded region, respectively).

robust estimate of N_H than those derived from a more restricted bandpass or made during the hard or intermediate states. This value is in agreement with the HI4PI Survey's measured N_H in the direction of J1727 (HI4PI Collaboration et al. 2016) and in reasonable agreement with the N_H values presented by K. Chatterjee et al. (2024) and J.-Q. Peng et al. (2024).

We also use an alternative relation, N_H (cm^{-2}) $= (2.87 \pm 0.04) \times 10^{21} A_V$ (mag) (H. Zhu et al. 2017, Equation (11)), rather than that of T. Güver & F. Özel (2009). This more recent relation is a more appropriate choice for estimating extinction, given it was determined by fitting the whole sample of the J. Wilms et al. (2000) abundances, which include XRBs. However, we note there is likely additional uncertainty due to the scatter observed in this relation (H. Zhu et al. 2017, Figure 9(a)). Assuming $R_V = 3.1$, we use Monte Carlo techniques and Equation (2) to instead estimate $E(B–V) = 0.27 \pm 0.01$ along the line of sight to J1727. This result, while dependent upon the choice of N_H and with likely greater uncertainty, is in agreement with our findings based on near-UV data and Galactic dust maps that $E(B–V) \lesssim 0.4$.

4.2.2. Suggested Distance to Swift J1727.8−1613

With $A_r = 0.84 \pm 0.06$ per Section 3.2, the remaining parameter values required for Equation (1) are the absolute and apparent r-band magnitudes, M_r and m_r, respectively. MS25 determine the donor star type to be K4(±1)V with $M_r = 6.6 \pm 0.5$ mag and $m_r = 21.13 \pm 0.05$ mag. Using these values produces the distance posterior distribution that we present in Figure 5 and a distance estimate of $5.5^{+1.4}_{-1.1}$ kpc, under the assumption that the donor star is a regular K4(±1)V star that has not lost significant mass during the binary evolution. In such a case, the distance would be reduced, implying reduced values of $E(B-V)$ and N_H.

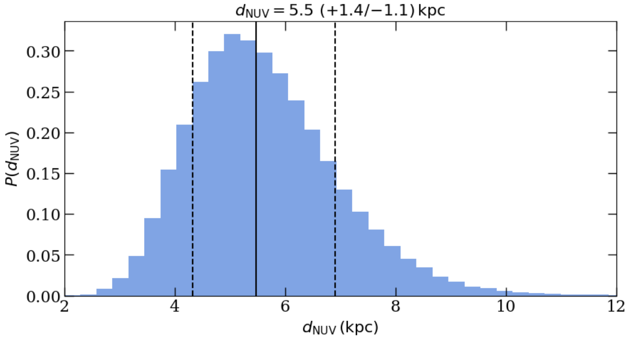

Figure 5. The distance posterior distribution produced from Monte Carlo calculations using the near-UV constraint on $E(B-V)$. The solid vertical line represents the 0.5000 quantile, and the dashed vertical lines represent the 0.1585 and 0.8415 quantiles.

(The data used to create this figure are available in the online article.)

4.2.3. Nature of the Donor Star

Using our distance estimate and the results from C. M. Wood et al. (2025), we define an upper limit on the inclination angle, i, for J1727 of $i \lesssim 69°$. To define a conservative lower limit on i, we assume an upper limit of $20\,M_\odot$ for the BH mass. It is likely that the BH is actually much smaller, as discussed with reference to high natal kick velocity in Section 4.3. We also use a maximum-entropy skew-normal distribution for the K4(±1)V donor star mass such that 1σ is contained within the range 0.70–0.78 $M_\odot$ and $\mu \approx 0.73\,M_\odot$. These mass values allow us to use the mass function provided by MS25,

$$f(M) \equiv \frac{M_1 \sin^3 i}{(1 + M_2/M_1)^2} = 2.77 \pm 0.09 M_\odot, \tag{3}$$

to estimate a 1σ lower limit of $i \geqslant 32.0 \pm 0.4°$.

MS25 obtained an upper limit of $v \sin i < 52\,\mathrm{km\,s^{-1}}$ for the rotational broadening of the donor star but recommend a more conservative 3σ upper limit of $102\,\mathrm{km\,s^{-1}}$ as this constraint is not especially strong. Values of $v \sin i > 102\,\mathrm{km\,s^{-1}}$ are therefore unlikely and would require $M_2 > 1 M_\odot$.

Given the binary system's orbital period, P_{orb}, and assuming that the donor star is tidally locked, the donor star's radius can be calculated as

$$R_2 = \frac{P_{\mathrm{orb}}(v \sin i)}{2\pi \sin i}. \tag{4}$$

MS25 directly measured $P_{\mathrm{orb}} = 10.8038 \pm 0.0010$ hr. Combining this with the $v \sin i = 27^{+25}_{-21}\,\mathrm{km\,s^{-1}}$ posterior distribution from MS25 and a uniform distribution of $\cos i \sim U(\cos 69°, \cos 32°)$ results in an R_2 distribution where $R_2 \ll 1.0\,R_\odot$, whereas K4($\pm$1) V stars typically have radii of $R \approx 1\,R_\odot$.

B. Paczyński (1967) relates the XRB orbital period and the mass and radius of a donor star undergoing Roche lobe overflow as

$$R_L \approx (2GM_2)^{1/3}(P_{\mathrm{orb}}/9\pi)^{2/3}, \tag{5}$$

where R_L is the Roche lobe radius, and M_2 is the donor star (secondary) mass. Taking $R_L = R_2$ as derived using the $v \sin i$ posterior distribution from MS25 results in an M_2 distribution that also favors extremely small, unphysical values ($M_2 \ll 0.1\,M_\odot$).

Donor stars of BH low-mass XRBs may be significantly evolved (P. Podsiadlowski et al. 2003; T. Fragos & J. E. McClintock 2015) and in Roche lobe overflow. However, there is no current evidence from the donor star spectral analysis by MS25 that it is significantly evolved or stripped, which would impact the distance estimate. Only with future, higher-resolution spectroscopic observations could we gain further information into the nature of the J1727 donor star.

We therefore infer that $v \sin i$ is unlikely to be as low as the MS25 posterior distribution might suggest. Assuming corotation and Roche lobe overflow, we again combine Equations (4) and (5). Then, using P_{orb} from MS25 and our aforementioned M_2 skew-normal and $\cos i$ uniform distributions, we calculate $v \sin i$ to be in the 3σ range 60–112 $\mathrm{km\,s^{-1}}$. This is roughly consistent with the MS25 3σ upper limit $v \sin i \lesssim 102\,\mathrm{km\,s^{-1}}$, given it is dependent upon conservative limits on i, and further contradicts the abundance of low values in the MS25 $v \sin i$ posterior.

4.3. Implications

4.3.1. Natal Kick Velocity and Birth Mechanism

Using their estimated distance of 3.4 ± 0.3 kpc, along with the proper motion of J1727, MS25 derived a median and 1σ confidence level in the potential natal kick velocity of $v_{\mathrm{kick}} = 210^{+40}_{-50}\,\mathrm{km\,s^{-1}}$. We use our suggested distance of $5.5^{+1.4}_{-1.1}$ kpc to provide an updated natal kick velocity of $190 \pm 30\,\mathrm{km\,s^{-1}}$ (P. Atri et al. 2019).[18] Our revised distance also corresponds to Galactic elevations of $z \approx 0.8$–1.2 kpc. We can compare this to XTE J1118+480, for which A. Gualandris et al. (2005) presented an asymmetric natal kick with a similar velocity of $183 \pm 31\,\mathrm{km\,s^{-1}}$ and a Galactic elevation of 1.9 ± 0.4 kpc. P. Atri et al. (2019) estimated a similar natal kick velocity for XTE J1118+480 and particularly high velocity kicks for other systems, such as 4U 1543−475, GS 1354−64, and SAX J1819.3−2525, and suggested that these are indicative of asymmetrical supernovae explosions as the likely birth mechanism. Applying this to J1727, it is possible that it could have been born within the Galactic disk and propelled by a natal kick to its present-day Galactic elevation. It is also possible that the large natal kick has caused a misalignment between the BH spin and the accretion disk for J1727 (T. J. Maccarone 2002; R. G. Martin et al. 2008). However, no evidence has been observed to date of precession of the jet axis (C. M. Wood et al. 2024, 2025).

4.3.2. Eddington Luminosity Fraction

A. A. Zdziarski et al. (2025) calculate an unabsorbed bolometric flux of $F_{\mathrm{bol}} \approx 5 \times 10^{-7}\,\mathrm{erg\,cm^{-2}\,s^{-1}}$ for J1727, as informed by the peak hard state flux from H.-X. Liu et al. (2024). At a distance of $5.5^{+1.4}_{-1.1}$ kpc, this would correspond to a luminosity of $L_{\mathrm{bol}} = 1.8^{+1.1}_{-0.7} \times 10^{39}\,\mathrm{erg\,s^{-1}}$. Assuming a nominal BH mass of $10\,M_\odot$, $L_{\mathrm{Edd}} \approx 1.3 \times 10^{39}\,\mathrm{erg\,s^{-1}}$, meaning an ELF of $L_{\mathrm{bol}}/L_{\mathrm{Edd}} \approx 1.4^{+0.9}_{-0.6}$ in this case. BHs with higher predicted natal kicks are expected to be less massive (e.g., K. Belczynski & T. Bulik 2002; T. J. Maccarone et al. 2020), yet reducing the BH mass would only increase this already-large ELF. Therefore, any distance within our 1σ uncertainties of 4.4–6.9 kpc is set to contravene expectations from A. A. Zdziarski et al. (2025), who note that the highest observed luminosities of low-mass XRBs in the hard or hard-intermediate states reside in the regime $L \lesssim 0.3\,L_{\mathrm{Edd}}$. A. A. Zdziarski et al. (2025) also noted that J1727 underwent a soft-to-hard-state transition at very low flux in the period 2024 February–April, at $F_{\mathrm{bol}} \approx 10^{-8}\,\mathrm{erg\,cm^{-2}\,s^{-1}}$. With this flux, our same distance corresponds to a soft-to-hard-state transition ELF of $0.029^{+0.016}_{-0.010}$ assuming a BH mass of $10\,M_\odot$, which is more in line with expectations of 1%–4% (E. Kalemci et al. 2013; A. Vahdat Motlagh et al. 2019). These ELFs imply that the distance to J1727 is likely on the lower end of our 1σ range. However, no single distance can satisfy the expectations on both the peak hard state luminosity and soft-to-hard-state transition luminosity. While ELFs from soft-to-hard-state transitions appear to be steadier (E. Kalemci et al. 2013), we caution that both the above ELFs are merely indicative and are unlikely to be reliable without a more accurate constraint on the BH mass.

5. Conclusions

Using H I absorption data from MeerKAT observations of the outburst of Swift J1727.8−1613, we determine a maximum absorption velocity of $24.8 \pm 2.8\,\mathrm{km\,s^{-1}}$. The higher-velocity absorption seen toward the extragalactic reference source PKS J1733−1304 allows us to use the near-kinematic distance as a lower bound of 3.6 ± 0.3 (stat) ± 2.3 (sys) kpc, accounting for the systematic uncertainty due to the low Galactic longitude of the source. However, its high Galactic latitude likely implies that we run out of H I clouds along the line of sight.

---

[18] https://github.com/pikkyatri/BHnatalkicks

Making use of a near-UV spectrum of Swift J1727.8−1613 as observed by the STIS on board HST, we measure the color excess or reddening to be $E(B-V)=0.37\pm0.01$ (stat) $\pm$ 0.025 (sys). This is significantly lower than previous constraints on $E(B-V)$ from MS24 and MS25), but it is in good agreement the maximum value derived from Galactic dust maps along this line of sight.

We use $E(B-V)$ to determine the r-band extinction, A_r, and combine this with donor star r-band magnitudes provided by MS25 for a K4(±1)V main-sequence donor star. Under this assumption, we subsequently present $5.5^{+1.4}_{-1.1}$ kpc as the resulting and likely distance to Swift J1727.8−1613, which implies a natal kick velocity of $v_{\rm kick}=190\pm30\,{\rm km\,s^{-1}}$ and suggests a likely formation in a natal supernova.

If the donor star has instead lost significant mass during the binary evolution, this distance would be smaller. However, the exact evolutionary stage and possible mass loss through accretion of the donor star is unknown. Further observations to better constrain binary inclination angle and the donor star rotational broadening would allow more accurate determination of the primary and secondary masses and consequently the distance.

Acknowledgments

The authors would like to thank James Allison for his development of the ThunderKAT H I Pipeline.

The authors would also like to thank Ilya Mandel, Ryosuke Hirai, Natasha Ivanova, and Thomas Maccarone for useful discussions.

The MeerKAT telescope is operated by the South African Radio Astronomy Observatory, which is a facility of the National Research Foundation, an agency of the Department of Science, Technology and Innovation.

We acknowledge the use of the ilifu cloud computing facility—https://www.ilifu.ac.za, a partnership between the University of Cape Town, the University of the Western Cape, Stellenbosch University, Sol Plaatje University and the Cape Peninsula University of Technology. The ilifu facility is supported by contributions from the Inter-University Institute for Data Intensive Astronomy (IDIA—a partnership between the University of Cape Town, the University of Pretoria and the University of the Western Cape), the Computational Biology division at UCT and the Data Intensive Research Initiative of South Africa (DIRISA).

This work made use of the Cube Analysis and Rendering Tool for Astronomy (CARTA) software (A. Comrie et al. 2024—https://cartavis.github.io).

This research is based on observations made with the NASA/ESA Hubble Space Telescope obtained from the Space Telescope Science Institute, which is operated by the Association of Universities for Research in Astronomy, Inc., under NASA contract NAS 5–26555. These observations are associated with program 16489.

N.C.S. acknowledges support from the Science and Technology Facilities Council (STFC) grant ST/X001121/1.

A.Z. acknowledges support from the Polish National Science Center grants 2019/35/B/ST9/03944 and 2023/48/Q/ST9/00138.

D.M.S. acknowledges support via a Ramón y Cajal Fellowship RYC2023-044941.

Facilities: MeerKAT, HST/STIS.

Software: ARVIZ (R. Kumar et al. 2019), ASTROPY (Astropy Collaboration et al. 2022), CASA (CASA Team et al. 2022), CARTA (A. Comrie et al. 2024), DUSTMAPS (G. Green 2018), JUPYTER (T. Kluyver et al. 2016), KD (T. V. Wenger 2018), MATPLOTLIB (J. D. Hunter 2007), MIRIAD (R. J. Sault et al. 1995), NUMPY (C. R. Harris et al. 2020), PRELIZ (A. Icazatti et al. 2023), PYMC (O. Abril-Pla et al. 2023), SCIPY (P. Virtanen et al. 2020), STISTOOLS (W. Hack et al. 2018).

ORCID iDs

Benjamin J. Burridge https://orcid.org/0009-0004-0093-0096
James C. A. Miller-Jones https://orcid.org/0000-0003-3124-2814
Arash Bahramian https://orcid.org/0000-0003-2506-6041
Steve R. Prabu https://orcid.org/0000-0003-3165-6785
Noel Castro Segura https://orcid.org/0000-0002-5870-0443
Jesús M. Corral-Santana https://orcid.org/0000-0003-1038-9104
Christian Knigge https://orcid.org/0000-0002-1116-2553
Andrzej Zdziarski https://orcid.org/0000-0002-0333-2452
Daniel Mata Sánchez https://orcid.org/0000-0003-0245-9424
Evangelia Tremou https://orcid.org/0000-0002-4039-6703
Francesco Carotenuto https://orcid.org/0000-0002-0426-3276
Rob Fender https://orcid.org/0000-0002-5654-2744
Payaswini Saikia https://orcid.org/0000-0002-5319-6620

References

Abdulghani, Y., Lohfink, A. M., & Chauhan, J. 2024, MNRAS, 530, 424
Abril-Pla, O., Andreani, V., Carroll, C., et al. 2023, PeerJ Comput.Sci., 9, e1516
Arnason, R. M., Papei, H., Barmby, P., Bahramian, A., & Gorski, M. D. 2021, MNRAS, 502, 5455
Astropy Collaboration, Price-Whelan, A. M., Lim, P. L., et al. 2022, ApJ, 935, 167
Atri, P., Miller-Jones, J. C. A., Bahramian, A., et al. 2019, MNRAS, 489, 3116
Atri, P., Miller-Jones, J. C. A., Bahramian, A., et al. 2020, MNRAS, 493, L81
Beardmore, A. P., Willingale, R., Kuulkers, E., et al. 2016, MNRAS, 462, 1847
Belczynski, K., & Bulik, T. 2002, ApJL, 574, L147
Bright, J., Farah, W., Fender, R., et al. 2023, ATel, 16228, 1
Camilo, F. 2018, NatAs, 2, 594
Cardelli, J. A., Clayton, G. C., & Mathis, J. S. 1989, ApJ, 345, 245
CASA Team, Bean, B., Bhatnagar, S., et al. 2022, PASP, 134, 114501
Castro Segura, N., Altamirano, D., Buisson, D., et al. 2020, HST Proposal, 16489
Castro-Tirado, A. J., Sanchez-Ramirez, R., Caballero-Garcia, M. D., et al. 2023, ATel, 16208, 1
Charles, P., Matthews, J. H., Buckley, D. A. H., et al. 2019, MNRAS, 489, L47
Chatterjee, K., Mondal, S., Singh, C. B., & Sugizaki, M. 2024, ApJ, 977, 148
Chauhan, J., Miller-Jones, J. C. A., Anderson, G. E., et al. 2019, MNRAS, 488, L129
Chauhan, J., Miller-Jones, J. C. A., Raja, W., et al. 2021, MNRAS, 501, L60
Chiang, Y.-K. 2023, ApJ, 958, 118
Comrie, A., Wang, K.-S., Hwang, Y.-H., et al. 2024, CARTA: The Cube Analysis and Rendering Tool for Astronomy v4.1.0, Zenodo, doi:10.5281/zenodo.15172686
Dhawan, V., Mirabel, I. F., Ribó, M., & Rodrigues, I. 2007, ApJ, 668, 430
Dickey, J. M. 1983, ApJL, 273, L71
Draghis, P. A., Miller, J. M., Homan, J., et al. 2023, ATel, 16219, 1
Dubus, G., Kim, R. S. J., Menou, K., Szkody, P., & Bowen, D. V. 2001, ApJ, 553, 307
Edenhofer, G., Zucker, C., Frank, P., et al. 2024, A&A, 685, A82
Fender, R., Woudt, P. A., Corbel, S., et al. 2016, in Proc. MeerKAT Science 277, On the Pathway to the SKA (Trieste: Sissa), 13
Fitzpatrick, E. L. 2004, in ASP Conf. Ser. 309, Astrophysics of Dust, ed. A. N. Witt, G. C. Clayton, & B. T. Draine (San Francisco, CA: ASP), 33
Fragos, T., & McClintock, J. E. 2015, ApJ, 800, 17
Gaia Collaboration, Prusti, T., de Bruijne, J. H. J., et al. 2016, A&A, 595, A1
Gandhi, P., Rao, A., Johnson, M. A. C., Paice, J. A., & Maccarone, T. J. 2019, MNRAS, 485, 2642
Green, G. 2018, JOSS, 3, 695

Green, G. M., Schlafly, E., Zucker, C., Speagle, J. S., & Finkbeiner, D. 2019, ApJ, 887, 93

Gualandris, A., Colpi, M., Portegies Zwart, S., & Possenti, A. 2005, ApJ, 618, 845

Güver, T., & Özel, F. 2009, MNRAS, 400, 2050

Hack, W., Dencheva, N., Sontag, C., Sosey, M., & Droettboom, M. 2018, STIS Python User Tools, https://stistools.readthedocs.io/en/latest/index.html

Harris, C. R., Millman, K. J., van der Walt, S. J., et al. 2020, Natur, 585, 357

Heinz, S., Burton, M., Braiding, C., et al. 2015, ApJ, 806, 265

HI4PI Collaboration, Ben Bekhti, N., Flöer, L., et al. 2016, A&A, 594, A116

Hunter, J. D. 2007, CSE, 9, 90

Hunter, G. H., Sormani, M. C., Beckmann, J. P., et al. 2024, A&A, 692, A216

Hynes, R. I., Haswell, C. A., Chaty, S., Shrader, C. R., & Cui, W. 2002, MNRAS, 331, 169

Icazatti, A., Abril-Pla, O., Klami, A., & Martin, O. A. 2023, JOSS, 8, 5499

Jonker, P. G., & Nelemans, G. 2004, MNRAS, 354, 355

Kalberla, P. M. W., & Kerp, J. 2009, ARA&A, 47, 27

Kalemci, E., Dinçer, T., Tomsick, J. A., et al. 2013, ApJ, 779, 95

Kluyver, T., Ragan-Kelley, B., Pérez, F., et al. 2016, Positioning and Power in Academic Publishing: Players, Agents and Agendas (Amsterdam: IOS Press), 87

Kumar, R., Carroll, C., Hartikainen, A., & Martin, O. 2019, JOSS, 4, 1143

Lamer, G., Schwope, A. D., Predehl, P., et al. 2021, A&A, 647, A7

Liu, H.-X., Xu, Y.-J., Zhang, S.-N., et al. 2024, arXiv:2406.03834

Lockman, F. J., Blundell, K. M., & Goss, W. M. 2007, MNRAS, 381, 881

Maccarone, T. J. 2002, MNRAS, 336, 1371

Maccarone, T. J., Osler, A., Miller-Jones, J. C. A., et al. 2020, MNRAS, 498, L40

Martin, R. G., Tout, C. A., & Pringle, J. E. 2008, MNRAS, 387, 188

Mata Sánchez, D., Muñoz-Darias, T., Armas Padilla, M., Casares, J., & Torres, M. A. P. 2024, A&A, 682, L1

Mata Sánchez, D., Torres, M. A. P., Casares, J., et al. 2025, A&A, 693, A129

Megier, A., Strobel, A., Galazutdinov, G. A., & Krełowski, J. 2009, A&A, 507, 833

Miller-Jones, J. C. A., Bahramian, A., Altamirano, D., et al. 2023a, ATel, 16271, 1

Miller-Jones, J. C. A., Bahramian, A., Orosz, J. A., et al. 2021, Sci, 371, 1046

Miller-Jones, J. C. A., Jonker, P. G., Dhawan, V., et al. 2009, ApJL, 706, L230

Miller-Jones, J. C. A., Sivakoff, G. R., Bahramian, A., & Russell, T. D. 2023b, ATel, 16211, 1

Mirabel, I. F., & Rodríguez, L. F. 1994, Natur, 371, 46

Munari, U., & Zwitter, T. 1997, A&A, 318, 269

Negoro, H., Serino, M., Nakajima, M., et al. 2023, ATel, 16205, 1

O'Connor, B., Hare, J., Younes, G., et al. 2023, ATel, 16207, 1

Paczyński, B. 1967, AcA, 17, 355

Peng, J.-Q., Zhang, S., Shui, Q.-C., et al. 2024, ApJL, 960, L17

Podsiadlowski, P., Rappaport, S., & Han, Z. 2003, MNRAS, 341, 385

Powell, C. R., Haswell, C. A., & Falanga, M. 2007, MNRAS, 374, 466

Reid, M. J. 2022, AJ, 164, 133

Reid, M. J., McClintock, J. E., Narayan, R., et al. 2011, ApJ, 742, 83

Reid, M. J., McClintock, J. E., Steiner, J. F., et al. 2014a, ApJ, 796, 2

Reid, M. J., Menten, K. M., Brunthaler, A., et al. 2014b, ApJ, 783, 130

Reid, M. J., Menten, K. M., Brunthaler, A., et al. 2019, ApJ, 885, 131

Reid, M. J., & Miller-Jones, J. C. A. 2023, ApJ, 959, 85

Rybarczyk, D. R., Wenger, T. V., & Stanimirović, S. 2024, ApJ, 975, 167

Sault, R. J., Teuben, P. J., & Wright, M. C. H. 1995, in ASP Conf. Ser. 77, Astronomical Data Analysis Software and Systems IV, ed. R. A. Shaw, H. E. Payne, & J. J. E. Hayes (San Francisco, CA: ASP), 433

Savage, B. D., & Mathis, J. S. 1979, ARA&A, 17, 73

Schlafly, E. F., & Finkbeiner, D. P. 2011, ApJ, 737, 103

Schlegel, D. J., Finkbeiner, D. P., & Davis, M. 1998, ApJ, 500, 525

Svoboda, J., Dovčiak, M., Steiner, J. F., et al. 2024, ApJL, 966, L35

Tetarenko, B. E., Sivakoff, G. R., Heinke, C. O., & Gladstone, J. C. 2016, ApJS, 222, 15

Vahdat Motlagh, A., Kalemci, E., & Maccarone, T. J. 2019, MNRAS, 485, 2744

Veledina, A., Muleri, F., Dovčiak, M., et al. 2023, ApJL, 958, L16

Virtanen, P., Gommers, R., Oliphant, T. E., et al. 2020, NatMe, 17, 261

Wallerstein, G., Sandstrom, K., & Gredel, R. 2007, PASP, 119, 1268

Wenger, T. V. 2018, tvwenger/kd v1.0, Zenodo, doi:10.5281/zenodo.1166001

Wenger, T. V., Balser, D. S., Anderson, L. D., & Bania, T. M. 2018, ApJ, 856, 52

Wilms, J., Allen, A., & McCray, R. 2000, ApJ, 542, 914

Wood, C. M., Miller-Jones, J. C. A., Bahramian, A., et al. 2024, ApJL, 971, L9

Wood, C. M., Miller-Jones, J. C. A., Bahramian, A., et al. 2025, ApJL, 984, L53

Woodgate, B. E., Kimble, R. A., Bowers, C. W., et al. 1998, PASP, 110, 1183

Zdziarski, A. A., Wood, C. M., & Carotenuto, F. 2025, ApJL, 986, L35

Zhu, H., Tian, W., Li, A., & Zhang, M. 2017, MNRAS, 471, 3494